Nuclear Science and Techniques (2023) 34:57
https://doi.org/10.1007/s41365-023-01212-4

Longitudinal impedance measurements and simulations of a three-metal-strip kicker

Jin-Liu Su[1,2] · Yu-Dong Liu[1] · Sai-Ke Tian[1] · Lei Wang[1] · Na Wang[1] · Sen Yue[1]

Received: 20 May 2022 / Revised: 7 December 2022 / Accepted: 18 December 2022 / Published online: 24 April 2023

Abstract
A kicker is a critical component for beam injection and accumulation in circular particle accelerators. A ceramic slat kicker plated with a TiN conductive coating was applied in the Beijing Electron Positron Collider (BEPCII). However, the ceramic slat kicker has experienced several sudden malfunctions during the operation of the BEPCII in the past. With a reliable kicker structure, a three-metal-strip kicker can substitute the original ceramic slat kicker to maintain the operational stability of the BEPCII. A comparison of the numerical simulation was conducted for three kicker models, demonstrating the comprehensive advantage of the three-metal-strip kicker. Furthermore, impedance bench measurements were conducted on a prototype of a three-metal-strip kicker. The longitudinal beam-coupling impedance was measured using a vector network analyzer via the coaxial wire method. A satisfactory agreement was obtained between the numerical simulations and measurements. Based on the numerical simulation data, the loss factor was 0.01721 V/pC, and the effective impedance was 3.59 mΩ ($\sigma = 10\,\mathrm{mm}$). The simulation of the heat deposition on each part of the kicker demonstrated that 84.4% of the parasitic loss of the beam was deposited on the metal strips, and the total heat deposition power on the kicker was between 113.3 and 131.5 W. The obtained heat deposition powers can be considered as a reference for establishing the cooling system.

Keywords Ceramic slat kicker · Three-metal-strip kicker · Impedance bench measurement · Coaxial wire method · Heat deposition power

1 Introduction

A ceramic slat injection kicker was proposed and applied to the BEPCII, which meets the requirements of the BEPCII storage ring injection system for a sufficient wide field region, high field uniformity, and low beam-coupling impedance. The detailed requirements for the injection kicker according to the BEPCII design report are listed in Table 1. At the top and bottom sides of the beam pipe, there are two long ceramic slats plated with a TiN conductive coating to provide a continuous image current. Its longitudinal length is approximately 1.7 m, and it is composed of two current buses and two ceramic slats, which can fix the current buses and support the TiN coating. The aperture of the kicker magnet is 90 mm × 44 mm. A TiN coating with a width of 34 mm was plated on the inner surface of the ceramic slats. The ceramic slat kicker sufficiently solved the contradiction between the beam impedance and field uniformity [1].

However, according to the BEPCII 2019 annual meeting proceedings, the ceramic slat injection kicker malfunctioned in April 2010 (e+k2), April 2011 (e−k2), December 2014 (e+k1), and August 2016 (e+k1). A possible reason for this failure is that the beam or synchrotron radiation directly hit the TiN coating, causing the coating to detach from the ceramic slat. Subsequently, the image current was blocked. A series of higher-order modes (HOM) was induced, resulting in an ignition inside the kicker. Consequently, the vacuum worsened, and the beam was lost.

To prevent coating detachment, three metal strips were chosen to replace the TiN-plated ceramic slat as the image

This was supported by the National Natural Science Foundation of China (Nos. Y8113C005C and U1832132).

✉ Yu-Dong Liu
liuyd@ihep.ac.cn

1 Institute of High Energy Physics, Chinese Academy of Sciences, Beijing 100049, China

2 University of Chinese Academy of Sciences, Beijing 100049, China

Table 1 Requirements for the injection kicker

Parameter	Value
Available length (m)	1.7
Beam stay clear (mm × mm) ($H \times W$)	38 × 82
Injection energy (GeV)	1.89
Deflection (mrad)	3
Integrated field strength (T m)	0.02
Bottom width of field waveform (ns)	600
Good field region (mm)	$X = \pm 20$
Field uniformity ($Y = 0$ mm plane)	± 1%
Field uniformity ($Y = 5$ mm plane)	± 2%
Field uniformity ($Y = 10$ mm plane)	± 5%

current path. To prevent the eddy current shielding effect and ensure magnetic field uniformity, two metal strips were disconnected from the middle with a slit of 1 mm.

Two important issues for the design of a kicker are the beam-coupling impedance and heat deposition on the kicker. The beam-coupling impedance can cause collective beam instabilities. To ensure a good beam quality and stable operation, the impedance of the components should be strictly limited. The heat load can cause localized heating, which may burn the components or destroy the vacuum in severe cases. Therefore, it is necessary to perform detailed impedance simulations of the three-metal-strip kicker. It is also useful to conduct bench measurements of impedance to verify the impedance simulations.

The remainder of this paper is organized as follows. The mechanical structure of the three-metal-strip kicker is described in Sect. 2. Section 3.1 presents a simplified CST model of kicker, an explanation of how it is simplified from the mechanical structure, and the difference between the simplified kicker model and another two CST models. Section 3.2 presents several formulae to describe the relationship between the wake function, wake potential, and impedance; the impedance simulation results of the three models are compared, and the possible source of narrow-band resonances is explained herein. Section 4.1 presents the coaxial wire measurement setup, measurement of the characteristic impedance with VNA-achieved TDR, conduction of another CST simulation to obtain the cutoff frequency of the kicker, comparison of the impedance between the simulations and measurements, explanation for the significantly large narrow-band resonance amplitudes of the measurements, and the calculated longitudinal loss factor and effective impedance. Section 5 presents the application of a module called time frequency power loss monitor in CST STUDIO SUITE to obtain the heat deposition power, and the simulation results are displayed. The conclusions are presented in Sect. 6.

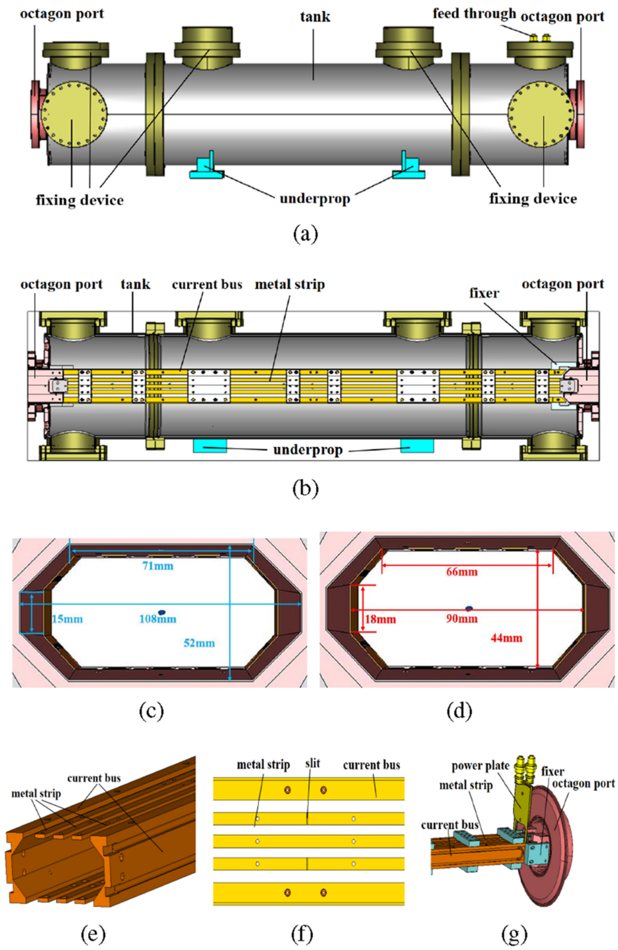

Fig. 1 (Color online) Mechanical structure of the three-metal-strip kicker: **a** side view, **b** longitudinal cross section along the beam axis, **c** outer dimensions of the kicker octagon port, **d** inner dimensions of the kicker octagon port, **e** zoomed transverse view of the metal strips, **f** zoomed top view of the metal strips, and **g** zoomed view of the power plates

2 Mechanical structure of the three-metal-strip kicker

With a longitudinal port-to-port length of 1706 mm and transverse tank width of 305 mm, the three-metal-strip kicker is quasi-symmetric, as shown in Fig. 1a, b. The two kicker octagon ports have the same dimensions, and the outer diameter (52 mm) is slightly larger than the inner diameter (44 mm), forming a longitudinal taper, as shown in Fig. 1c, d. The feedthrough was connected to the current buses through two power plates. Two long-current buses were located on both sides of the kicker. Two groups of three metal strips were located above and under the beam axis, functioning as the image current path. Among the three metal strips, two side strips have a slit of 1 mm in the middle, which ensures the maximum passage of the magnetic field, as shown in Fig. 1f. The gap between the strips is 8 mm wide and that between strip and current buses is 10 mm wide.

Owing to HOM heating, the metals of the kicker would be lengthened to a certain extent during operation with the beams. The metal strips should be carefully considered owing to the 1 mm slit. The fractional change in length is proportional to the change in temperature as follows:

$$\frac{\Delta L}{L} = \alpha \cdot \Delta T, \tag{1}$$

where $\Delta L/L$ is the fractional change in length, ΔT is the change in temperature, and α is the linear thermal expansion coefficient [2, 3]. Because the length change in the strips should be less than 1 mm, we obtain the following:

$$\frac{1}{2}(L_1 \cdot \alpha \cdot \Delta T + L_2 \cdot \alpha \cdot \Delta T) < 1\,\text{mm}, \tag{2}$$

where L_1 and L_2 are the strip lengths, as shown in Fig. 2. The linear thermal expansion coefficient of copper at a temperature of 20 °C was 17×10^{-6}/°C. Therefore, we found that the temperature of the metal strips should not exceed 99 °C; otherwise, the strips would touch each other during the operation with the beams. The temperature of the strips was determined based on the cooling system efficiency. Therefore, the heat deposition power on the strips is an important reference for establishing a cooling system.

3 Longitudinal impedance simulations and comparison

To acquire the complete information regarding the beam-coupling impedance, numerical simulations were performed using CST STUDIO SUITE [4]. The simulation results were also compared with those of two other models, illustrating that the three-metal-strip kicker is currently the most reliable model after considering the magnetic field uniformity, impedance, and operation stability comprehensively.

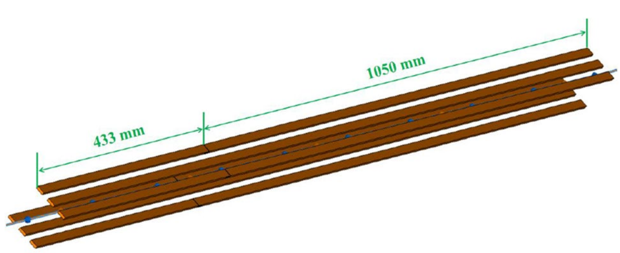

Fig. 2 (Color online) The dimensions of metal strips

3.1 Simulation models

A simplified model of the mechanical structure was applied to accelerate the simulation process. The underprop that supports the kicker below was deleted because it could not be seen by the beams. Screws, small holes, and fixing devices were deleted because they were shielded by the current buses and metal plates and did not have a significant effect on the beams. The outer parts of the kicker octagon ports and current buses were reshaped to be significantly smoother because they could not be seen by the beams. The cabling was not considered, and the power plates that connected the feedthrough with the current buses remained in the CST modeling. The fixer between the current buses and front octagon port was also modeled. A simplified structure of the three-metal-strip model is shown in Fig. 3.

The mesh sizes can be automatically adjusted by the CST software according to the specific dimension of a region. Adjustable mesh sizes can improve the calculation accuracy while saving the computing resources. In our calculations, a total of approximately 10^9 meshes were used for the three-metal-strip kicker. A Gaussian beam with an RMS bunch length of 10 mm was selected for the simulation. To improve the accuracy of the simulation results, the wakefields were tracked over 10m behind the bunch. Excluding the fixer connecting the current buses with the front kicker octagon port that was set as being composed of alumina, all other parts were set as being composed of a perfect electroconductive material (PEC).

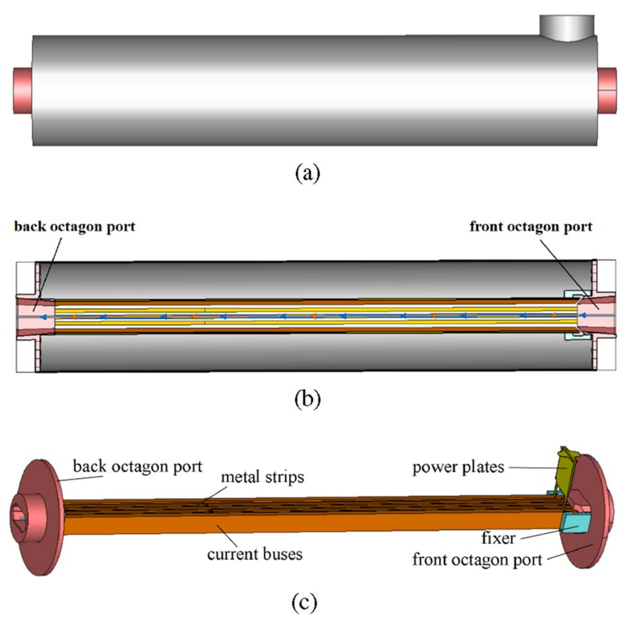

Fig. 3 (Color online) Simplified structure of the three-metal-strip model: **a** side view, **b** longitudinal cross section along the beam axis, **c** side view with the tank hidden

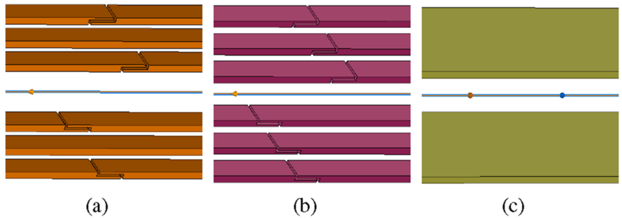

Fig. 4 (Color online) Structural differences between the three models: **a** three-metal-strip model, **b** fully-unconnected model, and **c** metal-slat model

Another model, called the fully unconnected model, is based on the three-metal-strip model, in which the only difference is that all its strips are unconnected with the same slit of 1 mm. The third model, the metal-slat model, is also based on the three-metal-strip model, in which the only difference is that the group of the three metal strips is combined as an entire metal slat. The structural differences between the three models are shown in Fig. 4.

3.2 Beam-coupling impedance

The longitudinal wake function in the CST software is defined as follows:

$$W'(z) = \frac{1}{q}\int_{-\infty}^{\infty} E_s(s)\mathrm{d}s, \tag{3}$$

where q is the excitation charge, E_s is the electric field along the s direction seen by the test charge, z is the distance at which the test charge is behind the excitation charge, and $W'(z)$ is the longitudinal wake function.

The longitudinal impedance $Z_{||}(\omega)$ can be calculated from the wake function $W'(z)$ using a Fourier transformation as follows:

$$Z_{||}(\omega) = -\int_{-\infty}^{\infty} \frac{1}{c} e^{-i\omega z/c} W'(z)\mathrm{d}z. \tag{4}$$

However, it is impossible to apply a point charge to perform the simulation. A bunch with a certain length and charge distribution was set up for the simulation. Therefore, the CST software provides data regarding the wake potential $V_{||}(z)$ rather than the wake function $W'(z)$. The relationship between the wake potential and wake function can be expressed as follows:

$$V_{||}(z) = \int_{-\infty}^{\infty} \lambda(\xi)W'(z-\xi)\mathrm{d}\xi, \tag{5}$$

where $\lambda(\xi)$ denotes the normalized line density of the bunch. The following is obtained by combining Eqs. (3) and (4):

$$Z_{||}(\omega) = -\frac{\int_{-\infty}^{\infty} V_{||}(z)e^{-i\omega z}\mathrm{d}z}{\int_{-\infty}^{\infty} \lambda(z)e^{-i\omega z}\mathrm{d}z}. \tag{6}$$

The wake potentials of the three models are shown in Fig. 5. The wake of the fully-unconnected model does not sufficiently decay to zero after 10 m. It must be a long-range wake owing to the gaps and slits. It is unnecessary to make the wake of the fully unconnected model sufficiently decay to zero after 10 m because it is only shown to compare the narrowband resonances. The wakes of the other two models decay to zero after 10 m.

The exact impedances can be obtained only if the wake potentials can be obtained for an infinite length or if they damp out completely over a finite length. Because the calculation of the wake potentials must be terminated at a certain length owing to the limitations of the computing resource, the impedance obtained from the simulations demonstrates oscillatory behavior around the actual resonance frequencies, and its real part may become negative at certain frequencies. To alleviate this problem, data windowing is applied, and a $\cos^2$ filtering function is selected in the CST software [4].

The real and imaginary parts of the longitudinal beam-coupling impedance of up to 2 GHz are shown in Fig. 6. This comparison illustrates that the narrowband resonances

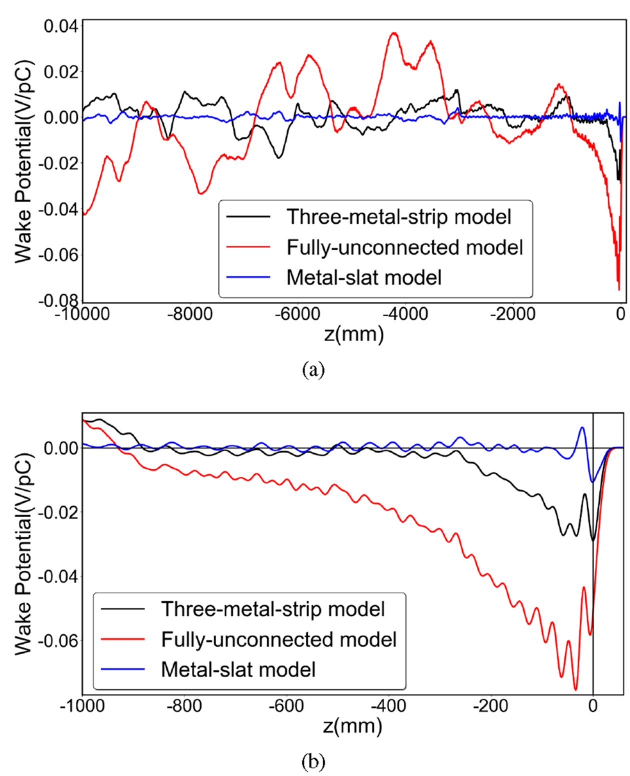

Fig. 5 (Color online) Wake potentials of the three models: **a** from −10,000 to 100 mm and **b** around $z = 0$

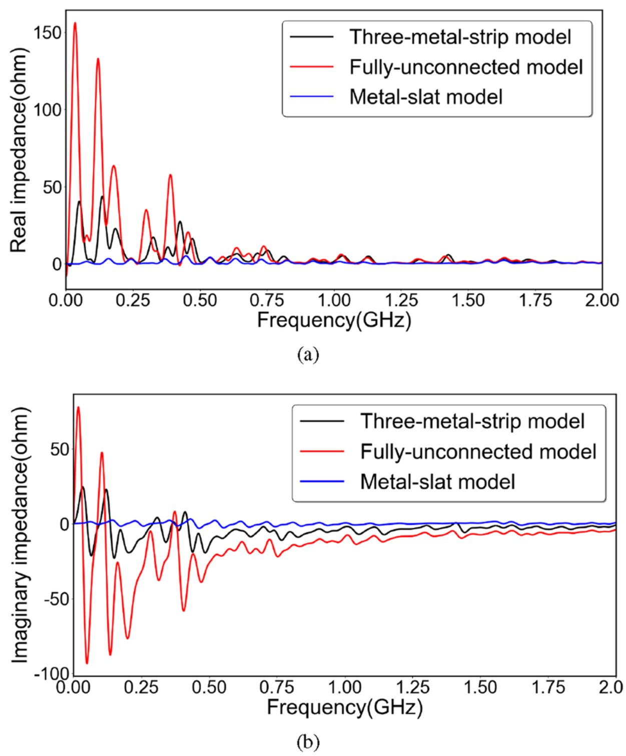

Fig. 6 (Color online) Comparison of the real (**a**) and imaginary part (**b**) of the longitudinal beam-coupling impedance between the three models

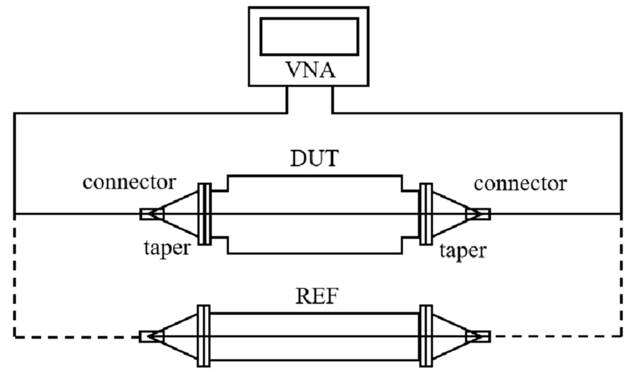

Fig. 7 Layout of the coaxial wire experimental setup

are caused by the tank. The diameter of the tank is 305 mm. Its cutoff frequency is approximately 1 GHz. The transverse dimension is sufficiently large to generate these resonances at low frequencies. The dimensions of the gaps and slits determine the effect of the tank. A greater number of gaps and slits lead to significantly higher resonances. The resonances of the fully unconnected model are significantly higher than those of the three-metal-strip model because the slits in the side strips of the fully unconnected model magnify the effect of the tank. The resonance amplitude of the metal-slat model is the smallest among these models because the metal slat weakens the effect of the tank. Impedance simulations and measurements of the ceramic slat kicker were conducted by Demin Zhou [5], demonstrating that its impedance is nearly the same as that of the three-metal-strip kicker.

Owing to the shielding effect produced by the eddy currents, the magnetic field cannot pass through the metal slat. Therefore, the metal-slat kicker, although demonstrating the lowest impedance, is not a suitable structure for the BEPCII. The fully unconnected model is also not a suitable structure owing to its large impedance. According to our measurements, the three-metal-strip kicker and ceramic slat kicker demonstrate similar performances with respect to the magnetic field. However, during the practical commissioning and operation of the BEPCII in the past 10 years, the accelerator breakdown caused by its TiN coating detachment occurred every three or four years. Therefore, the optimized three-metal-strip kicker with a lower longitudinal impedance and higher reliability may be the most suitable structure for the BEPCII owing to its apparent robustness against damage caused by heating.

4 Impedance bench experiment on a three-metal-strip kicker prototype

A prototype of the three-metal-strip kicker was manufactured to conduct an impedance bench experiment. The coaxial wire method was applied in the experiments, which has been widely used for the impedance bench measurements of the accelerator components [5–13]. In particular, Chinese investigators have conducted several pioneering studies regarding impedance measurements [5–9], which significantly benefited our experimental setup.

4.1 Coaxial wire measurement setup

The facilities for coaxial wire measurements include the VNA, tapers, device under test (DUT), and a smooth reference pipe (REF). The layout of the experimental setup is illustrated in Fig. 7. As shown in Fig. 8, the ports of the REF are the same as those of the DUT. The experimental bench is illustrated in Fig. 9. The taper developed by Huang et al. [14] is shown in Fig. 10. The N-type connectors, connecting blocks, and Teflon spacers are shown in Fig. 11. A copper wire with a diameter of 2 mm was used as the inner conductor. A combination of the copper wire on the beam axis with the connecting blocks, tapers, or DUT forms a coaxial wire that can be processed as a two-port network. Because the characteristic impedance of the coaxial cables and VNA, 50 Ω, is significantly different from that of the coaxial wire formed by the copper wire and DUT, this large

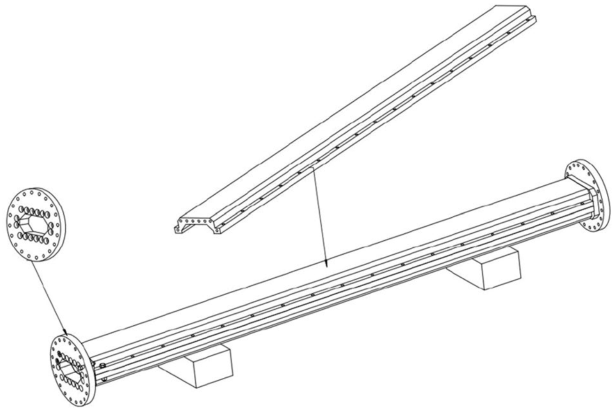

Fig. 8 The structure of REF

Fig. 9 (Color online) Snapshot of the coaxial wire experimental bench

Fig. 10 (Color online) Snapshot of the taper

impedance mismatch can cause a severe reflection, inducing ripples above the real impedance. To solve the mismatch problem, tapers are commonly used in the measurements.

Because the entire length of the structure, including the tapers, reaches approximately 3 m, and the end of the tapers

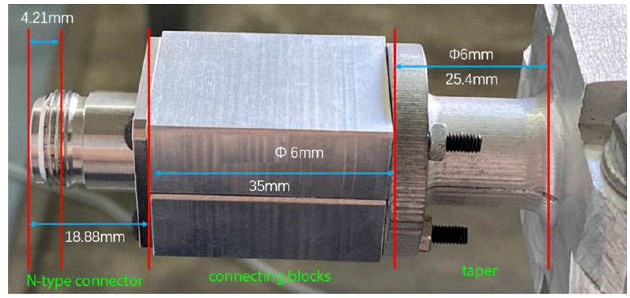

(a)

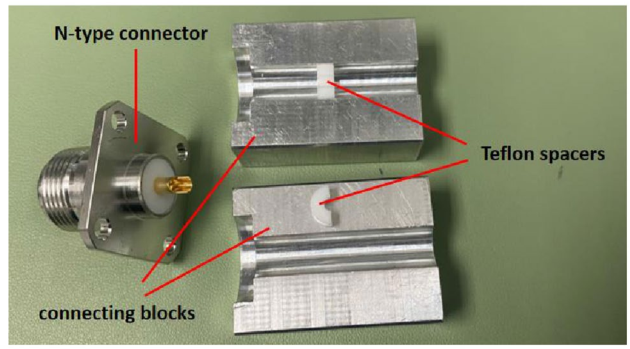

(b)

Fig. 11 (Color online) Snapshots of the N-type connector, connecting blocks, Teflon spacers, and taper

has a diameter of only 6 mm, stretching the copper wire along the beam axis [15] is significantly difficult. As a result, the measurement accuracy significantly decreases. In our measurement, we soldered the copper wire to an N-type connector with tin and used connecting blocks to cover the copper wire. Half-round Teflon spacers, as shown in Fig. 11, were placed inside the connecting blocks to fix the copper wire. The characteristic impedance, which changes with the distance along the coaxial wire, is shown in Fig. 13. The flatness in the middle of the curve indicates that the copper wire was sufficiently stretched to a certain extent.

To calculate the longitudinal beam-coupling impedance, the scattering coefficients S_{21} of the DUT and REF were measured using an Agilent E5071C ENA VNA. Subsequently, the impedance of the DUT can be calculated based on the scattering coefficients using the Hahn-Pedersen formula [16]:

$$Z_{||}(\omega) = 2Z_c\left(\frac{S_{21,\mathrm{REF}}}{S_{21,\mathrm{DUT}}} - 1\right), \tag{7}$$

or the Palumbo-Vaccaro formula [17]:

$$Z_{||}(\omega) = 2Z_c\left(1 - \frac{S_{21,\mathrm{DUT}}}{S_{21,\mathrm{REF}}}\right), \tag{8}$$

or using the Walling formula for a long DUT [18]:

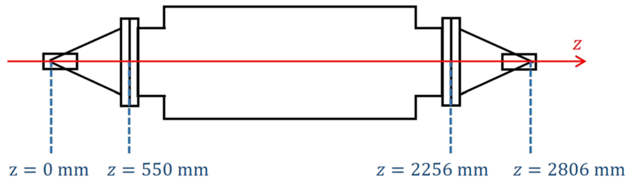

Fig. 12 Definition of the horizontal axis for the characteristic impedance curve

$$Z_{||}(\omega) = 2Z_c \ln\left(\frac{S_{21,\mathrm{REF}}}{S_{21,\mathrm{DUT}}}\right), \tag{9}$$

where Z_c is the characteristic impedance of the coaxial wire formed by the copper wire and DUT. The Walling formula was adopted for the experiment in this study.

The VNA-achieved TDR was applied to measure the characteristic impedance [19]. Because the travel speed of the incident signal is nearly equal to the speed of light, the location z can be expressed by $z = ct/2$. As shown in Fig. 12, the horizontal axis of the characteristic impedance curve is defined along the kicker center, and the zero point is set at the connector. The measured characteristic impedances of the DUT and REF are shown in Fig. 13.

In addition to the measurement, the characteristic impedance of the coaxial wire can also be estimated from the structural information using the following equation:

$$Z_c = \frac{1}{2\pi}\sqrt{\frac{\mu_0}{\epsilon_0}}\ln\frac{b}{a}, \tag{10}$$

where b is the outer conductor radius, a is the inner conductor radius, $\mu_0 = 4\pi \times 10^{-7}$ T·m / A, and $\epsilon_0 = 8.85 \times 10^{-12}$ F/m. Because the outer dimension of the kicker ports is slightly larger than the inner dimension, as shown in Fig. 1c, d, the TDR curve bulges at the location of the two kicker ports. Meanwhile, because there is a gap between the front port and the current buses, as shown in Fig. 14, a slight asymmetry in the TDR curve is induced. The REF ports are similar to that of the DUT; however, the DUT has a significantly more complicated structure. Therefore, the characteristic impedances of the REF and DUT would be the same at the octagon ports but different at other locations.

4.2 Benchmark between measurements and simulations

Because the cross section of the kicker port is octagonal, it is impossible to analytically calculate the cutoff frequency. As shown in Fig. 1c, d, the largest and smallest aperture dimensions are 108 mm and 44 mm, respectively. Therefore, we can obtain an approximate range for the cutoff frequency as follows:

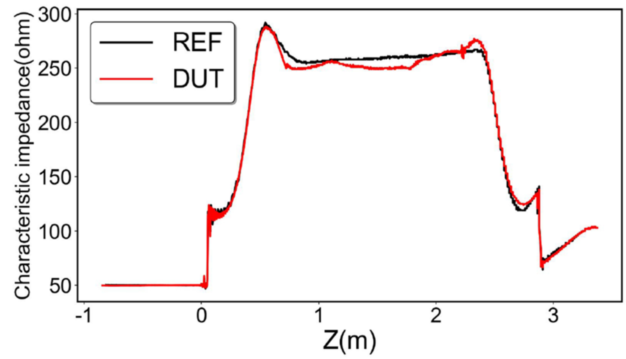

Fig. 13 (Color online) TDR-measured characteristic impedance over the distance along the coaxial wire

$$f_{\mathrm{min}} = \frac{c}{2\pi b_{\mathrm{max}}} = 0.88\,\mathrm{GHz}, \tag{11}$$

$$f_{\mathrm{max}} = \frac{c}{2\pi b_{\mathrm{min}}} = 2.17\,\mathrm{GHz}, \tag{12}$$

$$f_{\mathrm{avg}} = \frac{f_{\mathrm{min}} + f_{\mathrm{max}}}{2} = 1.53\,\mathrm{GHz}. \tag{13}$$

To obtain an accurate cutoff frequency value, we conducted another simulation using the CST software. As shown in Fig. 15a, one incident wave was set up to pass through a PEC tube that had the same cross section as the kicker. The frequency of the incident wave changed from 0 GHz to 5 GHz, and the dependence of the S-parameter on the frequency was recorded, as shown in Fig. 15b. The S_{21} curve illustrates that the cut-off frequency is approximately 1.61 GHz.

As the cutoff frequency of the kicker is approximately 1.61 GHz, the real and imaginary parts of the longitudinal impedance are displayed up to 2 GHz. The results are compared with those obtained from the CST simulations. The comparison in Fig. 16 illustrates that the kicker longitudinal impedance mainly exists in the low-frequency range. The narrow-band resonances of the bench measurement and simulation were located at nearly the same frequencies. However, the resonance amplitude of the bench measurement

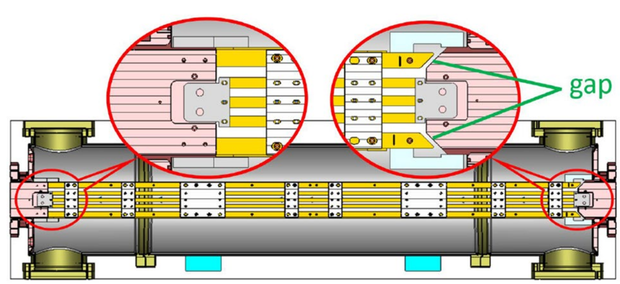

Fig. 14 (Color online) Gap between the front port and current buses

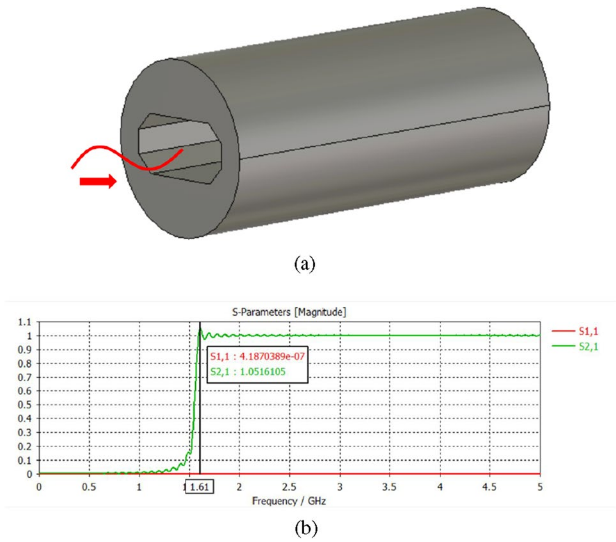

Fig. 15 (Color online) Simulation for determining the cutoff frequency of the kicker port: **a** simulation setting and **b** obtained dependence of S_{21} on the frequency

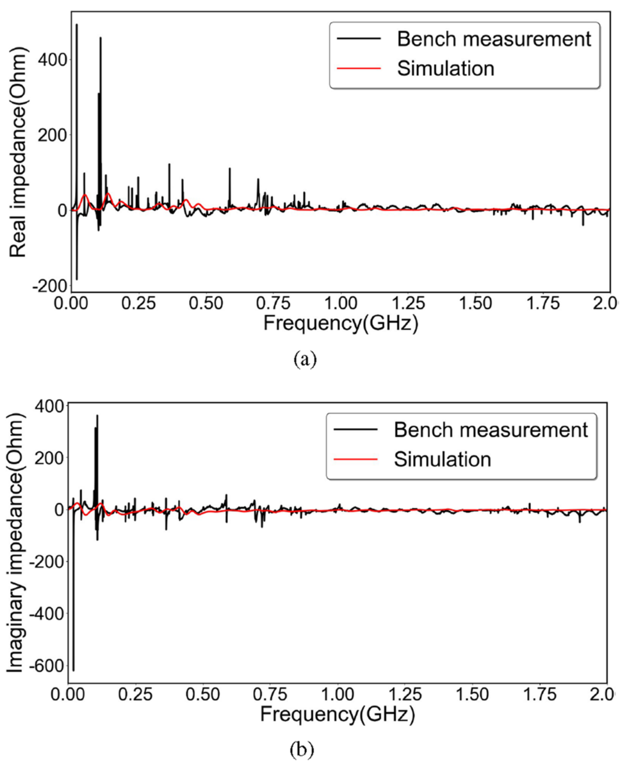

Fig. 16 (Color online) **a** Real and **b** imaginary parts of the longitudinal impedance measured by the coaxial wire method and compared with simulations

was significantly larger. This may be caused by the multiple reflections owing to the impedance mismatch. No absorber was used in the measurements. Uncertain HOMs are induced owing to the multiple reflections. Their frequencies may be equal to or near the frequencies of the narrow-band resonances. Subsequently, the resonance amplitudes were magnified. To verify this hypothesis, we plan to deposit absorbers in the tapers and select a copper wire with a diameter of 3 mm by referring to Lambertson et al. [20].

Based on the impedance spectrum shown in Fig. 16, the loss factor was calculated within different frequency ranges ($\sigma = 10\,\mathrm{mm}$), as shown in Fig. 17. Based on the bench measurements, the loss factor up to 2 GHz was 0.01723 V/pC and the longitudinal effective impedance $\frac{Z_{||}}{n}$ up to 2GHz was 5.45 mΩ ($\sigma = 10\,\mathrm{mm}$). Based on the simulations, the loss factor up to 2 GHz was 0.01721 V/pC, and the longitudinal effective impedance $\frac{Z_{||}}{n}$ up to 2 GHz was 3.59 mΩ ($\sigma = 10\,\mathrm{mm}$). These data demonstrate good consistency between the measurement and simulation results. Furthermore, the loss factor for the ceramic slat kicker was 0.017±0.002 V/pC based on the measurements in a previous study by Demin Zhou [5], which is significantly close to the value indicated above.

5 Heat deposition on different parts of three-metal-strip kicker

As a beam passes through the kicker, it loses a certain amount of energy. The energy loss is called the parasitic loss of the beam and can be calculated using the following equation:

$$\Delta W_{\mathrm{beam}} = q^2 k_{||}, \tag{14}$$

where q is the bunch charge and $k_{||}$ is the longitudinal loss factor [21]. An energy loss occurred only during the passage, which was a relatively short time. The parasitic power loss over one turn of the storage ring can be calculated as follows:

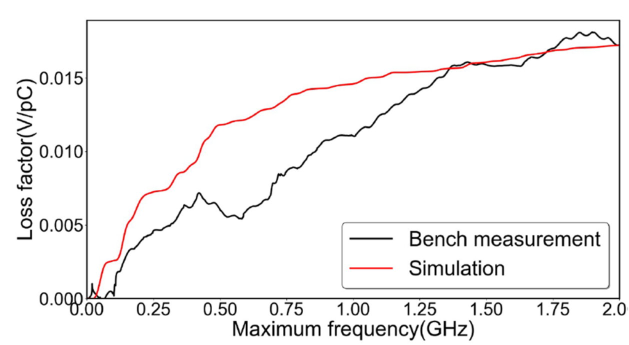

Fig. 17 (Color online) Longitudinal loss factor within different frequency ranges

$$P_{\text{beam}} = q^2 k_{||} f_{\text{r}}, \tag{15}$$

where f_{r} denotes the revolution frequency. The variable P_{beam} is a certain value determined by the Kicker impedance, which is independent of time. Note that $k_{||}$ is calculated using frequencies up to the kicker cutoff frequency. Certain modes with frequencies higher than the kicker cutoff frequency can travel out of the kicker and eventually deposit their energy on lossy materials elsewhere. Only modes with frequencies lower than the kicker cutoff frequency trapped inside the kicker are considered herein [22, 23]. However, once the beam travels into the kicker, the electromagnetic field begins to continually deposit energy on the kicker. After passage of the beam, the HOM trapped in the kicker continues to deposit energy on the kicker until all the parasitic energy lost by the beam is deposited. Therefore, the heat deposition power P_{beam} is a continuous function of time and can be obtained through simulations.

As the total energy is conserved, the following relationship between P_{beam} and P_{heat} exists:

$$\Delta W_{\text{beam}} = \int_0^{T_{\text{r}}} P_{\text{beam}} \mathrm{d}t = \int_0^{T_{\text{end}}} P_{\text{heat}} \mathrm{d}t, \tag{16}$$

where T_{r} is the revolution period and T_{end} is the heat deposition duration.

To obtain the heat deposition power on each part of the kicker, a module called the time frequency power loss monitor in CST STUDIO SUITE was used [4].

In the simulation, the bunch charge, bunch RMS length, and wakefield tracking length were 1 nC, 10 mm, and 50 m, respectively. Because the heat deposition power is proportional to the square of the bunch charge, and the bunch charge in the BEPCII is 7.78 nC (9.8 mA), the final simulation results were multiplied by the square of 7.78, as shown in Figs. 18 and 19.

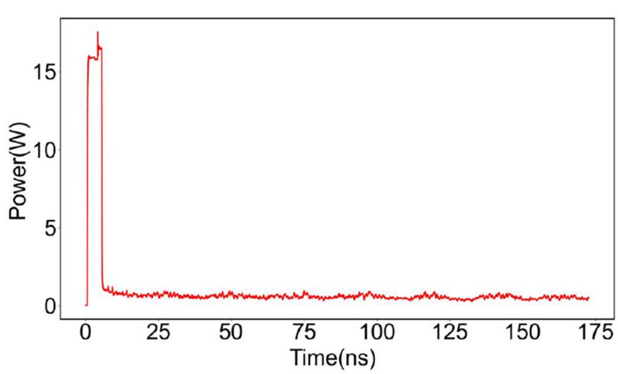

Fig. 18 Total heat deposition power on the kicker based on the CST simulation

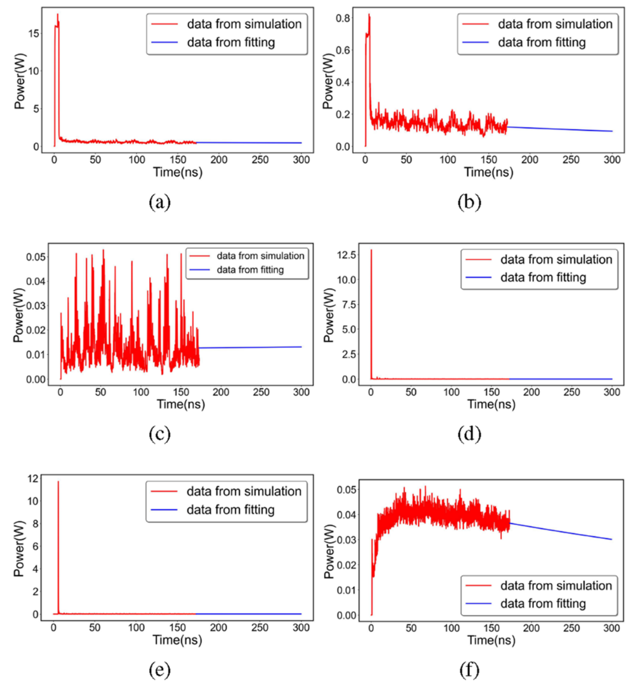

Fig. 19 (Color online) Heat deposition power on each part of the kicker based on the CST simulation and data fitting: **a** metal strips, **b** current buses, **c** power plates, **d** front port, **e** back port, and **f** side wall

The practical heat deposition process prolongs for an extremely long duration, whereas the simulation process only lasts 175 ns owing to the limited time and computing resources. Data fitting was performed to obtain more information regarding the deposition. To improve the data fitting results, all the data of the power plates and 98.29–172.75 ns data of the other parts of the kicker were used. An exponential function was chosen as the fitting function to describe the decay process of the deposition. The heat deposition curves over time, including a part of the fitted data, are shown in Fig. 19.

To obtain the deposited energy proportion for each part of the kicker, the heat deposition power should be integrated to infinity over time. The energy deposited on each part of the kicker is shown in Table 2, which demonstrates that approximately 84% of all the parasitic energy lost by the beam was deposited on the metal strips.

The aforementioned discussions are based only on a single bunch passing through the kicker, whereas a storage ring contains multiple bunches. There were 93 bunches in the BEPCII, the bunch current was 9.8 mA, and the revolution time was 791.77 ns. Therefore, the time interval between the two bunches is 791.77 ns divided by 93, that is, 8.51 ns. To obtain the final heat deposition power generated by multiple bunches, the heat deposition power of the bunch should be overlaid with those of the later bunches. The results after approximately 10 turns are shown in Fig. 20.

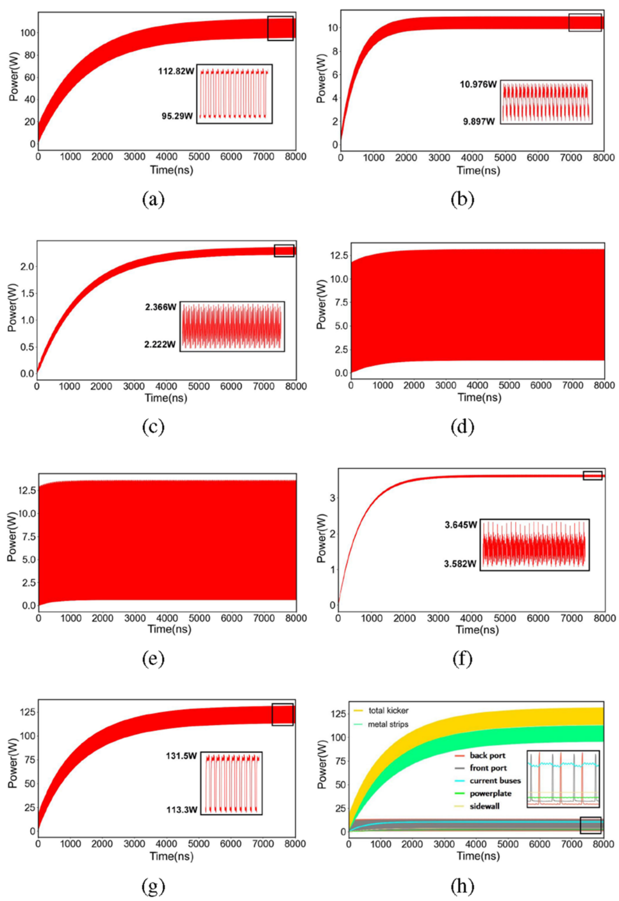

Fig. 20 (Color online) Heat deposition power on each part of the kicker after overlying approximately 10 turns: **a** metal strips, **b** current buses, **c** power plates, **d** front port, **e** back port, **f** side wall, **g** entire kicker, and **h** comparison

Figure 20 illustrates that after the heat deposition power of one bunch is overlaid with others, the final deposition power on each part of the kicker oscillates within a range. The power range rises rapidly and reaches a stable region after approximately 10 turns. The lower limit, upper limit, and average powers of each part of the kicker are listed in Table 3, which demonstrates that among all the parts of the kicker, the metal strips have the largest power and require more consideration.

The heat deposition data can be further processed by obtaining the average. Considering 8.51 ns as the smallest time unit, the average deposition power can be calculated for each time unit and designated as the instantaneous deposition power in the middle of the time unit. The final averaged heat deposition powers over time for each part of the kicker are shown in Fig. 21. The final convergent power averages are presented in Table 3.

The parasitic power loss of the beam over one turn can be calculated using $P_{\mathrm{beam}} = n_{\mathrm{b}} q^2 k_{\|} f_{\mathrm{r}}$. The measured longitudinal impedance provides the loss factors 0.01723 V/pC and P_{beam}=122.50 W. The CST simulation yields the loss factors 0.01721 V/pC and P_{beam}=122.35 W, respectively. The direct CST simulation of the heat deposition on the kicker provides the average heat deposition power of 124.63 W, which is consistent with the parasitic power loss of the beam.

6 Conclusion

After comprehensively considering the beam-coupling impedance, magnetic field uniformity, heat deposition on the kicker owing to the parasitic loss of the beam, and operational stability, the three-metal-strip kicker is determined to be the most suitable structure for the BEPCII. The impedance and loss factor of the three-metal-strip kicker are nearly the same as those of the ceramic-slat kicker. The impedance simulations and bench measurements of the kicker prototype using the coaxial wire method were in good agreement. The heat deposition power on the kicker obtained from the CST simulations sufficiently matches the beam parasitic loss power calculated from the loss factor. The final heat deposition power on each part of the kicker can be considered as a reference for designing the cooling system.

Table 2 Energy deposited on each part of the kicker

Part	Simu. energy (J)	Fit energy (J)	Total energy (J)	Proportion (%)
Current buses	2.7103×10^{-8}	6.2350×10^{-8}	8.9455×10^{-8}	8.41
Metal strips	1.7490×10^{-7}	7.2265×10^{-7}	8.9758×10^{-7}	84.36
Power plates	2.2722×10^{-9}	1.7268×10^{-8}	1.9540×10^{-8}	1.84
Back port	6.4081×10^{-9}	3.8535×10^{-9}	1.0262×10^{-9}	0.96
Front port	6.8252×10^{-9}	9.6337×10^{-9}	1.6459×10^{-8}	1.55
Sidewall	6.6581×10^{-9}	2.4038×10^{-8}	3.0696×10^{-8}	2.89
Kicker	2.2416×10^{-7}	8.3977×10^{-7}	1.0640×10^{-7}	100

Table 3 Convergence range of the heat deposition power on each part of the kicker after approximately 10 turns

Part	Min. power (W)	Max. power (W)	Avg. (W)
Current buses	9.897	10.976	10.51
Metal strips	95.29	112.82	105.08
Power plates	2.222	2.366	2.29
Back port	0.57	13.72	1.21
Front port	1.28	13.20	1.93
Sidewall	3.582	3.645	3.61
Kicker	113.3	131.5	124.63

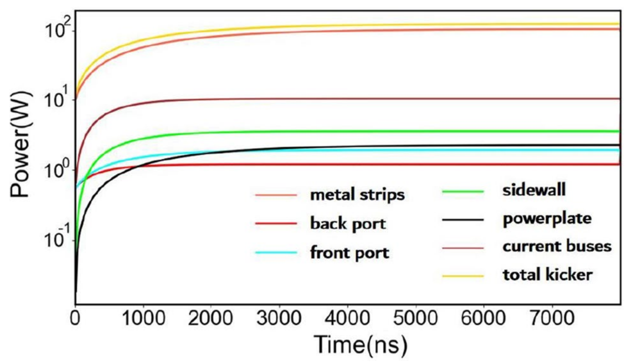

Fig. 21 (Color online) Averaged heat deposition power on each part of the kicker with a log scale after overlying approximately 10 turns

Acknowledgements We would like to thank the IHEP accelerator team for their support and discussions, particularly, the kicker team for providing an accurate mechanical drawing of the kicker and patient explanation.

Author Contributions All authors contributed to the study conception and design. Material preparation, data collection and analysis were performed by Jin-Liu Su, Yu-Dong Liu, Sai-Ke Tian, Lei Wang, Na Wang, and Sen Yue. The first draft of the manuscript was written by Jin-Liu Su and all authors commented on previous versions of the manuscript. All authors read and approved the final manuscript.

Data availability The data that support the findings of this study are openly available in Science Data Bank at https://www.doi.org/10.57760/sciencedb.07738 and http://resolve.pid21.cn/31253.11.sciencedb.07738.

References

1. W. Kang, Y.D. Hao, Q. Han et al., A new slotted-pipe kicker magnet for BEPCII storage ring, in *Proceedings of PAC 2005, Knoxville, Tennessee* (2005), pp. 955–957. https://doi.org/10.1109/PAC.2005.1590623
2. N.K. Rajak, N. Kondedan, H. Jan et al., Setup of high resolution thermal expansion measurements in closed cycle cryostats using capacitive dilatometers. J. Phys. Commun. **5**, 125004 (2021). https://doi.org/10.1088/2399-6528/ac3a44
3. B.D. Dunn, Materials and Processes. (Springer, Chichester, 2016), Appendix 1: Coeffcient of (Linear) Thermal Expansion for Selected Materials (COE or CTE). https://doi.org/10.1007/978-3-319-23362-8
4. CST STUDIO SUITE website. http://www.cst.com
5. D.M. Zhou, Longitudinal impedance calculations and measurements of vacuum components for BEPCII storage rings, Dissertation, IHEP (**in Chinese**) (2005)
6. G.W. Wang, Measuring the longitudinal impedance of components in the BEPC storage ring, Ph.D. thesis, IHEP (**in Chinese**) (1989)
7. Y.B. Leng, Development and Experiment of Longitudinal Impedance Measurement System, Ph.D. thesis, USTC (**in Chinese**) (1999)
8. G. Huang, The study of longitudinal coupling impedance measurement and beam feedback system, Ph.D. thesis, Tsinghua University (**in Chinese**) (2002)
9. D.M. Zhou, J.Q. Wang, L.J. Zhou et al., Longitudinal impedance measurement of the components for the BEPCII, in *Proceedings of PAC 2005, Knoxville, Tennessee* (2005), pp. 3212–3214. https://doi.org/10.1109/PAC.2005.1591416
10. N. Wang, S.K. Tian, L. Wang et al., Impedance optimization and measurements of the injection stripline kicker. Phys. Rev. Accel. Beams **24**, 034401 (2021). https://doi.org/10.1103/PhysRevAccelBeams.24.034401
11. M. Kumar, L.K. Babbar, R.K. Deo et al., Modified coaxial wire method for measurement of transfer impedance of beam-position monitors. Phys. Rev. Accel. Beams. **21**, 052801 (2018). https://doi.org/10.1103/PhysRevAccelBeams.21.052801
12. C. Vollinger, F. Caspers, T. Kaltenbacher, Coaxial wire method adapted to weakly coupled resonator mode for LHC RF fingers evaluation, in *Proceedings of IPAC 2016, Busan, Korea* (2016), pp. 3670–3672. https://doi.org/10.18429/JACOW-IPAC2016-THPMY009
13. E. Ergenlik, D. Le Guidec, P. Lepercq et al., Transverse impedance coaxial wire measurement in an extended frequency range, in *Proceedings of IPAC 2021, Campinas, SP, Brazil* (2021), pp. 4227–4230. https://doi.org/10.18429/JACoW-IPAC2021-THPAB222
14. G. Huang, D.M. Zhou, J.Q. Wang et al., Development of longitudinal coupling impedance measurement platform for BEPCII, in *Proceedings of PAC 2005, Knoxville, Tennessee* (2005), pp. 1940–1942. https://doi.org/10.1109/PAC.2005.1590965
15. J.D. Yuan, J.X. Wu, B. Zhang et al., Investigation of factors affecting vertical sag of stretched wire. Nucl. Sci. Tech. **32**, 20 (2021). https://doi.org/10.1007/s41365-021-00847-5
16. H. Hahn, F. Pedersen, On coaxial wire measurements of the longitudinal coupling impedance, Report No. BNL 50870 (1978)
17. A. Argan, L. Palumbo, M.R. Masullo et al., On the Sands and Rees measurement method of the longitudinal coupling impedance, in *Proceedings of PAC 1999, New York* (1999), pp. 1599–1601
18. L.S. Walling, D.E. McMurry, D.V. Neuffer et al., Transmission line impedance measurements for an advanced hadron facility. Nucl. Instrum. Methods Phys. Res. Sect. A **281**, 433 (1989). https://doi.org/10.1016/0168-9002(89)91474-5
19. T. Dennis, Broadband Measurement Techniques for Impedance Spectroscopy and Time Domain Reflectometry Applications (Cuvillier Verlag, 2013), pp. 100–125
20. G. Lambertson, A. Jacob, R. Rimmer et al., Techniques for beam impedance measurements above cutoff, in *Proceedings of EPAC 1990, Nice, France* (1990), pp. 1049–1051
21. A.W. Chao, Lectures on Accelerator Physics (World Scientific, 2020), pp. 822–823

22. J.J. Guo, Q. Gu, M. Zhang et al., Power losses caused by longitudinal HOMs in 1.3 GHz cryomodule of SHINE. Nucl. Sci. Tech. **30**, 105 (2019). https://doi.org/10.1007/s41365-019-0628-9
23. M.X. Liu, C.F. Wu, Y.G. Tang et al., Design and calculation of a side-coupled accelerating structure. Nucl. Sci. Tech. **28**, 160 (2017). https://doi.org/10.1007/s41365-017-0309-5